Chemical Engineering Journal 461 (2023) 141889

Contents lists available at ScienceDirect

Chemical Engineering Journal

journal homepage: www.elsevier.com/locate/cej

Novel isoreticular UiO-66-NH_2 frameworks by *N-cycloalkyl* functionalization of the 2-aminoterephtalate linker with enhanced solar photocatalytic degradation of acetaminophen

Almudena Gómez-Avilés [a], Rafael R. Solís [a,b,*], Eva M. García-Frutos [c], Jorge Bedia [a], Carolina Belver [a]

[a] Chemical Engineering Department, Universidad Autónoma de Madrid, Campus Cantoblanco, E-28049 Madrid, Spain
[b] Chemical Engineering Department, Universidad de Granada, Campus Fuentenueva, E-18001 Granada, Spain
[c] Instituto de Ciencia de Materiales de Madrid, CSIC, Campus Cantoblanco, E-28049 Madrid, Spain

ARTICLE INFO

Keywords:
UiO-66-NH_2
Linker functionalization
Photocatalysis
Water treatment
Acetaminophen

ABSTRACT

This work reports for the first time the functionalization of the 2-aminoterephtalate linker of UiO-66-NH_2 with cyclopentyl or cyclohexyl rings. The resulting materials displayed reduced bandgaps with enhanced separation of the photogenerated charges due to the inductive electron effect of the cycloalkyl substituent. These functionalized materials displayed higher photocatalytic performance towards the solar abatement of acetaminophen than UiO-66-NH_2. The photocatalytic activation mechanism was proposed based on the band alignment and scavenger tests, suggesting the major contribution of holes and superoxide radicals. In particular, UiO-66-NH-C_5 exhibited high stability under reaction with low activity loss after reusing. The acetaminophen degradation pathway was also studied indicating that the ACE molecules were coupled to dimers and trimers that were further oxidized. The small bandgap, the band structure, and the photocatalytic performance resulting from the cycloalkyl functionalization of UiO-66-NH_2 make it a promising approach to designing novel photocatalysts for solar abatement of emerging contaminants.

1. Introduction

Metal Organic Frameworks (MOFs) represent a novel generation of crystalline materials built by polymeric coordinated bindings between an inorganic secondary building unit, namely metal clusters, and organic molecules acting as linkers [1]. Multiple organic molecules can serve as the linker, the most popular being carboxylates, phosphonates, sulfates, azole, and heterocyclic compounds [2]. The modification of the linker enables the modulation of the structure, porosity, and electronic properties of the MOF, enlarging their potential applications. Among them, currently it is under research their application in gas storage, such as hydrogen [3,4] and carbon dioxide [5], gas separation [6,7], water remediation [2,8], catalysis in a wide range of reactions [9,10], energy storage [11,12], drug delivery [13–15] or sensing [16,17]. Within heterogeneous catalysis, photocatalysis is a potential application of MOFs since the early 2000's due to their semiconductor properties. The removal of organic molecules, hydrogen production, CO_2 reduction, and water splitting are some examples of photocatalytic processes [18]. Essentially, photocatalysis is based on the conversion of light into chemical energy. This process is labeled as an environmentally friendly technology as only a light source and a solid semiconductor are needed and can operate under mild ambient-like conditions. One of the most important driving forces that currently supports the use of photocatalysis is the possibility of using solar radiation as a light source. Sunlight, like renewable energy, exemplifies a low-cost and green alternative with the highest feasible potential. Thus, MOFs have gained attention in solar photocatalysis since MOFs can be activated by irradiation transferring electrons from the organic linker to the unoccupied d-orbitals of the metal cluster by a mechanism known as ligand-to-metal charge transfer (LMCT) [19,20]. Among the most used MOFs, Fe-based (as MIL-53, -88 and -101), Ti- (MIL-125), Zr- (UiO-66), and Zn-MOFs (ZIF-8) are the most popular, and all their derivatives have been described to enhance the solar light harvesting [21–24].

The zirconium-based UiO-66 MOF [25] is the scaffolding result from the combination of the cubic framework of cationic $Zr_6O_4(OH)_4$ nodes and terephthalic acid molecules as linker, concretely, via 12-

* Corresponding author at: Chemical Engineering Department, Universidad de Granada, Campus Fuentenueva, E-18001 Granada, Spain.
E-mail address: rafarsolis@ugr.es (R.R. Solís).

https://doi.org/10.1016/j.cej.2023.141889
Received 20 October 2022; Received in revised form 19 January 2023; Accepted 11 February 2023
Available online 14 February 2023

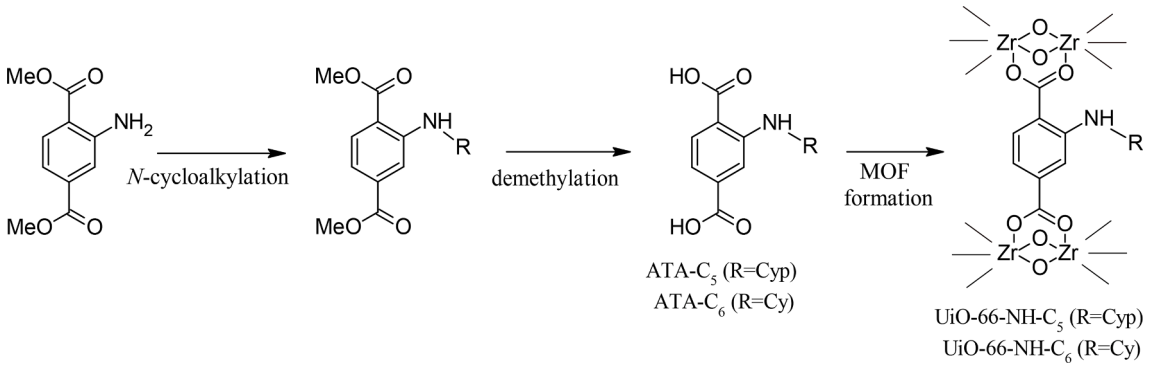

Fig. 1. Synthesis of the *N*-cycloalkyl-2-aminoterephthalic acids and the amino functionalized UiO-66-NH_2.

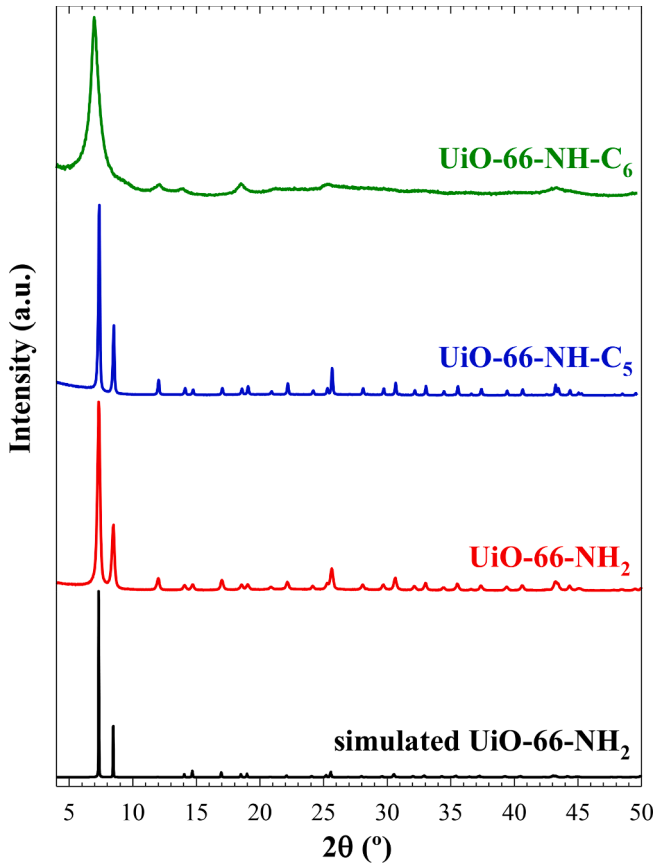

Fig. 2. XRD patterns of all samples.

coordinated bonds [26]. This high coordination has been proved to make UiO-66 very stable under a wide range of thermal conditions and diverse types of solvents, water included [8]. Zr-based MOFs have revealed outstanding stability in aqueous solution due to the strong Zr-O bonds and their specific geometry that minimizes the inclusion of water molecules which helps to mitigate undesirable hydrolysis reactions [25]. Moreover, the Zr_6-cluster can be reversibly rearranged upon removal or addition of hydroxyl groups, without any alterations in the connecting carboxylates [25]. Based on the exceptional stability of the UiO-66 structure, diverse modifications on the linker have extended the UiO-66 family. From the diverse attempts to functionalize the aromatic ring of the terephthalate linker tested to the date [27–29], the use of 2-amino-terephthalic acid (ATA) has led to enhanced harvesting of the solar light in the visible region [30–32]. The further functionalization of the amino group in ATA has recently been reported with very good results in MIL-125(Ti)-NH_2 [33]. Hence, a gradual red shift in the light absorption was achieved with the functionalization of *N*-alkylated derivatives, linear, reticular, and cyclic. The cyclic derivate led to a stronger electronic induction from the linker to the metal cluster, thus reducing the bandgap of the resulting photocatalyst [33]. The post-synthetic grafting of MIL-125(Ti)-NH_2 with heterocyclic carboxaldehydes also resulted in a reduction of the bandgap, yielding new photocatalysts for water treatment [34].

Based on the previous premises regarding the (i) stability of the UiO-66 family in water, (ii) the enhanced visible light absorption based on the antenna effect by the amino group, and (iii) the benefits of the *N*-alkyl-amino functionalization to reduce even more the bandgap energy and induce electron-donor mobility; several *N*-cycloalkyl-amino functionalized UiO-66-NH_2 have been prepared. Two *N*-cycloalkyl-amino modified linkers have been synthesized, ATA-cyclopentyl (ATA-C_5) and ATA-cyclohexyl (ATA-C_6) for preparing their Zr-MOFs versions, UiO-66-NH-C_5 and UiO-66-NH-C_6, respectively. It should be remarked that this approach has not been previously reported, which confirms the novelty of this study. The prepared materials have been fully characterized by diverse techniques, with special attention to the electrochemical and optical properties. Next, the benefits of the *N*-cycloalkyl functionalization were proved for photocatalytic degradation under simulated solar radiation of a contaminant of emerging concern in water, i.e. acetaminophen, which is frequently reported in sewage effluents [35,36]. The study also analyses the photocatalytic performance of the novel *N*-cycloalkyl functionalized UiO-66-NH_2, confirming its remarkable enhancement and stability. Special attention was paid to understanding the radical mechanism and the degradation pathway.

2. Experimental section

2.1. Chemicals

All chemicals used were analytical grade at least, acquired from Merck® and used without further purification. Solvents and silica gel 60, 0.04–0.06 mm for flash chromatography were acquired from Scharlau-Scharlab. Reactants and silica gel on TLC Al foils, type 60 with fluorescent indicator 254 nm were purchased from Sigma-Aldrich. The acetonitrile used for the chromatographic analysis was HPLC grade (Scharlab). All the stock solutions were prepared using ultrapure water (resistivity, 18.2 MΩ cm).

2.2. Synthesis of N-cycloalkyl functionalized UiO-66-NH_2 (UiO-66-NH-C_5 and UiO-66-NH-C_6)

2.2.1. Synthesis of N-cycloalkyl-2-aminoterephthalate dimethyl ester

The general procedure synthesis of *N*-cycloalkyl-2-amino-terephthalate dimethyl esters was performed following a previous work [33], see the steps in Fig. 1. Under N_2 atmosphere, 2-aminoterephthalate dimethyl ester was suspended in anhydrous *N,N*-dimethylformamide

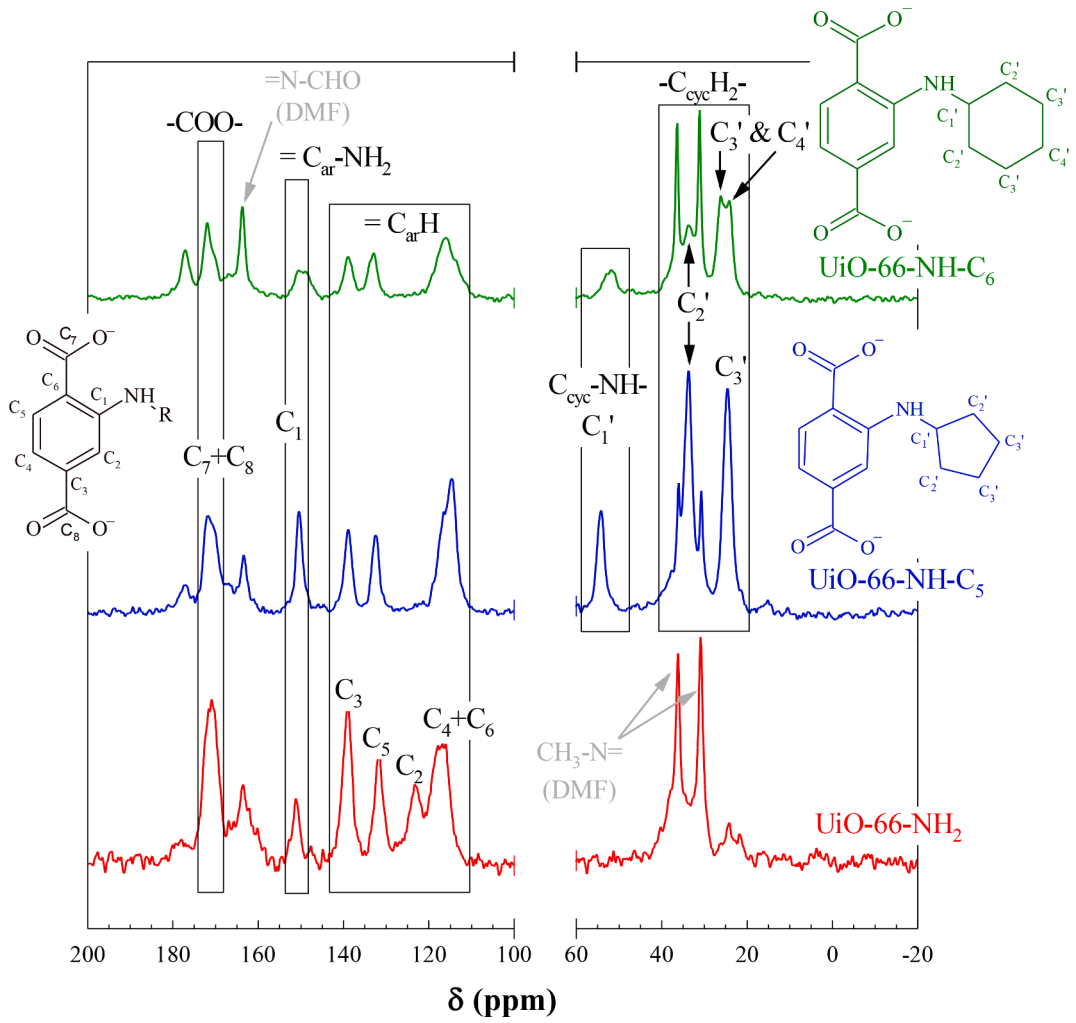

Fig. 3. ^{13}C solid-state NMR spectra of UiO-66-NH$_2$ and *N*-cycloalkylfunctionalized UiO-66-NH$_2$ samples.

(DMF), and stirred until complete dissolution. After, trimethylsilyl chloride (TMSCl) and the corresponding cyclic ketone (cyclopentanone and cyclohexanone) were added to the above solution and the mixture cooled down to 0 °C. Next, $NaBH_4$ was incorporated slowly over 5 min. The resulting mixture was warmed up to room temperature until the reaction was fully completed. The mixture was then quenched with a solution of saturated $NaHCO_3$ (aq.) and the resulting product was extracted with ethyl acetate. The organic fractions were washed thereafter with brine and dried over $MgSO_4$, filtered and the solvent was removed in a rotary evaporator.

2.2.2. *Synthesis of N-cycloalkyl-2-aminoterephthalic acids*

The general procedure synthesis of *N*-cycloalkyl-2-amino-terephthalic acid was performed following a previous work [33], see the steps in Fig. 1 The *N*-cycloalkylated dimethyl ester obtained was dissolved in tetrahydrofuran (THF), followed by the addition of NaOH 1 M. The resultant solution was heated under stirring to 70 °C for 8 h. The mixture was concentrated in a rotary evaporator at 45 °C to remove the excess THF. The concentrated was cooled down to room temperature and HCl 1 M was added until set pH = 3. The collected precipitate was isolated by filtration, washed with water, and dried. Two different *N*-cycloalkyl-2-aminoterephthalic acids were obtained i.e., the cyclopentyl (ATA-C_5) and the cyclohexyl (ATA-C_6) derivates.

2.2.3. *Synthesis of the N-cycloalkyl-amino functionalized UiO-66-NH$_2$*

The MOF UiO-66-NH$_2$, the functionalized UiO-66-NH-C_5, and UiO-66-NH-C_6 were prepared by solvothermal method following an adapted synthesis from the literature [29]. Briefly, 1.5 mmol of the linker, i.e. ATA, ATA-C5, or ATA-C6, was dissolved in 43 mL of DMF and placed, under vigorous stirring, in a Teflon lined vessel of 75 mL. Then, 1.5 mmol of $ZrOCl_2{\cdot}8\,H_2O$ was added to the above DMF solution. Next, 7 mL of acetic acid and 286 μL of HCl (37 %) were added. After homogenization, the vessel was hermetically closed and heated at 140 °C for 16 h. The crystallized yellowish solids were recovered by centrifugation (9000 rpm, 5 min) and washed twice with DMF and water. The resulting solids were dried under vacuum overnight (16 h, 80 °C), collected, and ground.

2.3. *Compounds and materials characterization*

The structure of the synthesized *N*-cycloalkyl-2-amino terephthalic acids was verified by different techniques. Nuclear magnetic resonance (NMR) spectra were performed on a Bruker AVANCE 300 MHz spectrometer for ^{1}H (300 MHz, DMSO-d_6) and ^{13}C (75.4 MHz, DMSO-d_6). The Fourier transform infrared (FTIR) spectra were recorded within 4000–250 cm^{-1} with a resolution of 1 cm^{-1} in a Bruker© VERTEX 70v IR instrument. Detailed results and discussion are provided in the Supplementary material (Figs. S1–S5). Molecular mass was determined by matrix-assisted laser desorption/ionization and time of flight mass spectrometry (MALDI-TOF) in a ULTRAFLEX III spectrometer from Bruker. The calculated error of the *m/z* values was −1.60 ppm for [ATA-C_5 + H]$^+$ and −1.30 ppm for [ATA-C_6 + H]$^+$.

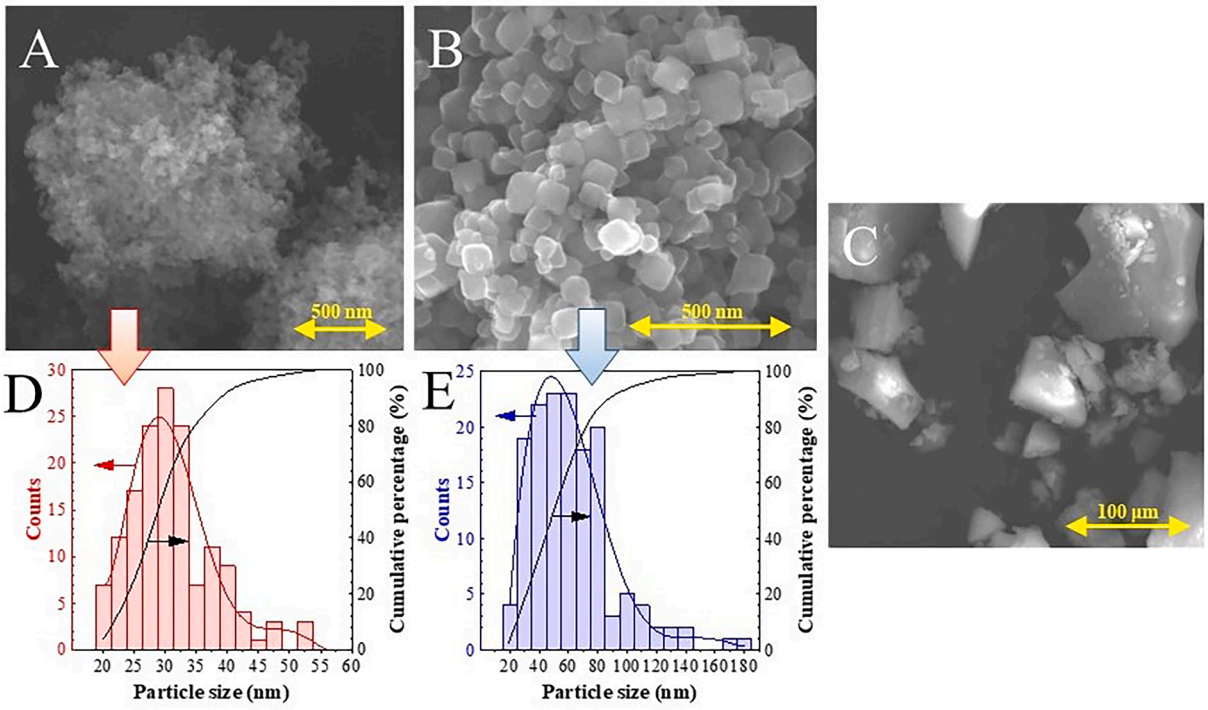

Fig. 4. SEM pictures of UiO-66-NH_2 (A), UiO-66-NH-C_5 (B), and UiO-66-NH-C_6 (C). Particle size distribution of UiO-66-NH_2 (D) and UiO-66-NH-C_5 (E).

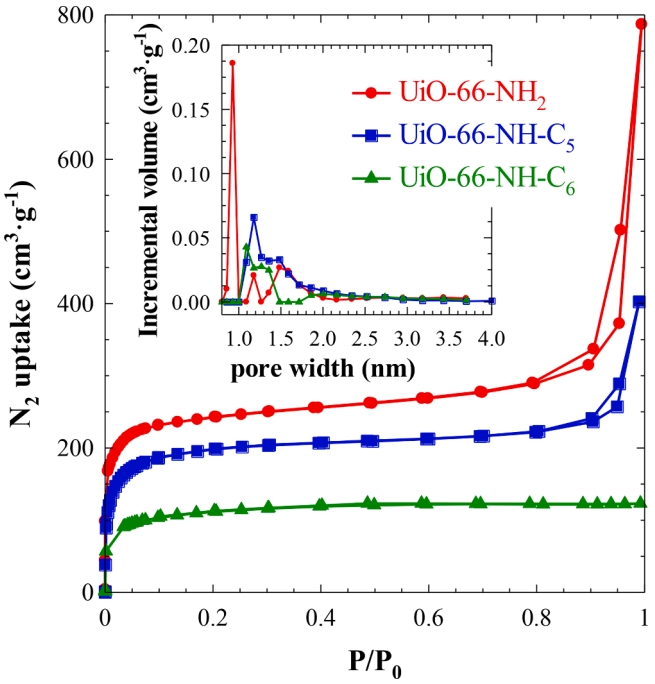

Fig. 5. N_2 adsorption–desorption isotherms and pore size distribution (inlet).

The solid-state X-ray diffraction (XRD) patterns were acquired on a Bruker D8 Advance diffractometer equipped with a Cu Kα1 source and a Lynxeye XE-T detector, recording the 2θ range within 4–50° at scan step of 1.8 min^{-1}. The software *Match!*® was used to process the XRD diffractograms and the XRD pattern of the UiO-66-NH_2 standard (CCDC-1405751) was simulated with Vesta®. ^{13}C solid-state NMR spectra were acquired on a Bruker AV-400-WB spectrometer (100.61 MHz) using Kel-F plugged ZrO rotors at room temperature. Recording conditions were set as 10 kHz spinning frequency, 35 kHz spectral width, 3 ms contact time and 4 s relaxation time. Scanning electron microscopy (SEM) was performed on a Quanta 3D FEG (de FEI^{TM} Company) and Hitachi S-4800 devices. The software *ImageJ* was used to measure the particle size and determine the particle size distribution. The surface area and porosity were assessed by N_2 adsorption–desorption at –196 °C in a TriStar 123 apparatus (Micromeritics). The specific surface area was calculated by the BET method (S_{BET}), the *t*-plot method was used to determine the surface area of micropore (S_{MP}) and the volume of micropore (V_{MP}). Total pore volume (V_T) was calculated from the N_2 uptake at P/P_0 = 0.99. UV–visible diffuse reflectance spectroscopy (DRS) was carried out to assess the optical properties in a Shimadzu UV2600 spectrophotometer equipped with an integrating sphere. The Tauc plot method was applied to estimate the bandgap of the materials considering indirect transitions [27], estimating the Kubelka–Munk function ($F(R_\infty)$) and depicting $(F(R_\infty)\cdot h\nu)^{1/2}$ vs the energy of the absorbed photons [37,38]. The electrochemical properties of the different materials were conducted in a Metrohm Autolab potentiostat (PGSTAT204) using three-electrode (DropSens ITO10) displayed in a Faraday cage (Methrom). Each sample was suspended (1 mg mL^{-1}) in aqueous 0.5 M Na_2SO_4, as a supporting electrolyte (pH 6.9–7.2 at 25 °C), and located in the electrochemical cell. Electrochemical impedance spectroscopy (EIS) was registered within 10^5 to 10^{-1} Hz at a fixed potential of –1.2 V. The flat

Table 1
Characteristic parameters of the porous texture.

Sample	S_{BET} (m^2 g^{-1})	S_{MP} (m^2 g^{-1})	S_{EXT} (m^2 g^{-1})	S_{MP}/S_{BET} (%)	V_T (cm^3 g^{-1})	V_{MP} (cm^3 g^{-1})	V_{MP}/V_T (%)
UiO-66-NH_2	798	585	213	73.3	1.218	0.281	23.1
UiO-66-NH-C_5	655	458	198	70.0	0.623	0.218	35.0
UiO-66-NH-C_6	371	229	144	61.7	0.190	0.109	56.8

S_{BET}: specific surface area; S_{MP}, micropores specific surface area; S_{EXT}: external specific surface area; V_T: total pore volume; V_{MP}: volume of micropore.

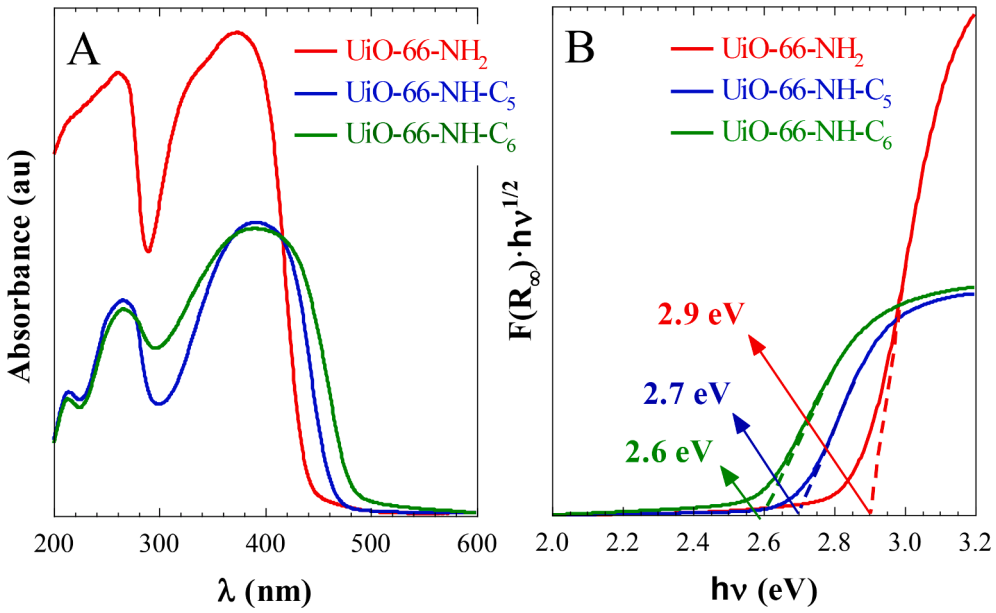

Fig. 6. UV–visible DRS absorption spectra (A) and the corresponding Tauc plots for the calculation of their bandgap energy (B).

Table 2
Optical and electronic properties.

Sample	E_g (eV)	$V_{FB\ (NHE,\ pH)}$ (V)	V_{CB} (V)	V_{VB} (V)
UiO-66-NH_2	2.9	−0.80	−0.62	2.28
UiO-66-NH-C_5	2.7	−0.80	−0.66	2.04
UiO-66-NH-C_6	2.6	−0.80	−0.68	1.92

E_g: bandgap energy; V_{FB}, flat band potential NHE corrected at pH = 7; V_{CB}: conduction band potential; V_{VB}: valence band potential.

band potential (V_{fb}) was obtained from the Mott-Schottky plot under a voltage between −1.5 and 0.4 V at 100 Hz. This value was from the intersection of the tangent with the abscissa axis (potential) in the representation of $1/C^2$ (C, the capacitance of the semiconductor-electrolyte junction) vs applied potential (V) [39]:

$$\frac{1}{C^2} = \frac{2}{\varepsilon \bullet \varepsilon_0 \bullet e \bullet N_D} - \left(V - V_{fb} - \frac{k \bullet T}{e}\right) \quad (1)$$

where $V_{fb\ (NHE,\ pH)}$ stands for the flat band potential at the pH medium, ε and ε_0 mean the permittivity of the semiconductor and the void, respectively; e is the electron charge; k the Boltzmann's constant; and T the temperature. The conduction band potential (V_{CB}) was obtained respect to the normal hydrogen electrode (NHE) at pH 7 according to a Nernstian shift considering the redox potential of Ag/AgCl ($\Delta V_{Ag/AgCl}$ = 0.21 V) [40]:

$$V_{CB} = V_{fb(Ag/Agcl,\ pH)} + \Delta V_{(Ag/Agcl,\ NHE)} \Delta 0.059 \cdot (7 \Delta pH) \quad (2)$$

Finally, the valence band potential (V_{VB}) can be estimated accounting the bandgap value (E_g) as follows:

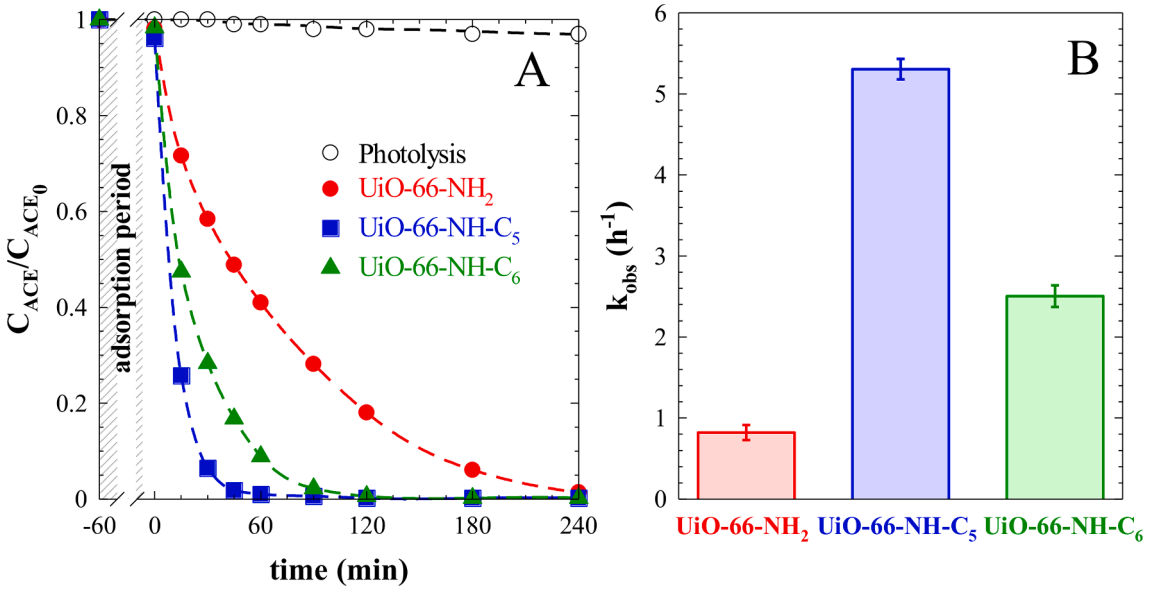

Fig. 7. Time-course evolution of the normalized concentration of ACE during the photocatalytic degradation (A) and the calculated pseudo-first order rate constants (B). *(V = 250 mL; $C_{ACE,0}$ = 5 mg L^{-1}, C_{CAT} = 250 mg L^{-1}; T = 25 °C, pH_0 = 4.2 ± 0.2).*

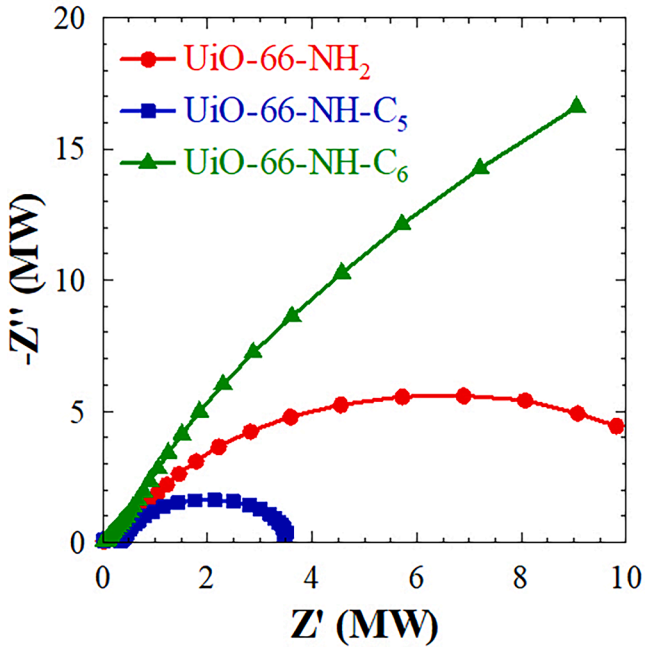

Fig. 8. EIS Nyquist plots.

$$V_{VB} = V_{CB} + \frac{E_g}{e} \quad (3)$$

2.4. Photocatalytic tests

The photocatalytic activity of the prepared MOFs was assessed for the abatement of acetaminophen (ACE) in water. For the degradation tests, a solar simulator device was used, Suntest XLS+ (ATLAS) equipped with a Xe lamp, and emitting radiation over 320 nm (indoor ID65 filter) at 600 W m^{-2}. A 250 mL glass reactor, jacketed with cooling water at 25 °C, was located inside the simulator device. The photodegradation tests were preceded by 1 h of an adsorption equilibrium step (under darkness). Next, the lamp of the simulator was switched on and samples were taken. The aqueous suspensions were filtered with PTFE syringeless filters (Whatman, 0.2 μm) for HPLC analysis and PTFE syringe filters (Whatman, 0.45 μm) for Total Organic Carbon (TOC) and Ionic Chromatography (IC) analysis. The ACE concentration was quantified by high-performance liquid chromatography in a Shimadzu Prominence-i LC-2030C HPLC, equipped with a diode array detector (SPD-M30A). The stationary phase was a C18 Eclipse Plus column (4.6 × 150 mm, 5 μm, Agilent) kept at 40 °C. The mobile phase pumped at 0.7 mL min^{-1} consisted of a mixture of aqueous acetic acid solution (0.1 % v/v, A) and acetonitrile (B). A gradient program of initially A:B = 90:10 to 60:40 in 10 min was used. The injection volume was 30 μL and the detection wavelength used was selected to 246 nm. The lixiviation of the organic linkers in the reaction medium was determined by the same chromatographic method. ATA was quantified at 392 nm while the wavelength was set at 236 nm for ATA-C_5 and ATA-C_6. Triplicate tests were carried out and the average represented lower than 5 % of the relative standard deviation.

Quenching experiments were carried out with 2-propanol (1 mM) as $HO^{\bullet}$ quencher, oxalic acid (10 mM) to trap h^+, p-benzoquinone (p-BQ) (0.1 mM), and tiron (1 mM) to quench $O_2^{\bullet-}$, and $AgNO_3$ (1 mM) as e^- quencher. The presence of hydroxyl radical was also assessed by a probe method based on the selective oxidation of terephthalic acid (TA) into 2-hydroxy-terephthalic acid (2-OH-TA), whose presence can be quantified by fluorescence spectroscopy [41–43]. A photocatalytic test in the presence of 2 mM of sodium terephthalate was conducted to probe the presence of $HO^{\bullet}$. The analysis of the 2-OH-TA produced was measured in a Varian Cary Eclipse fluorescence spectrophotometer. The excitation wavelength was set at 315 nm and the quantification was conducted at an emission set of 428 nm, correlating the peak intensity with 2-OH-TA concentration. All the quenching tests were conducted following the same procedure above described with the addition of the chemical quencher after the previous adsorption of the catalyst and pH adjustment with NaOH/HCl solution to the initial pH of the blank test.

The byproducts formed during ACE degradation were identified by liquid chromatography coupled to electrospray ionization-mass spectrometry (LC-ESI-MS) in a Bruker MaXis-II instrument under ESI working in positive ionization. The acquisition conditions were as follows: 3500 V capillary voltage, 8 mL min^{-1} dry gas flow, dry heater at 300 °C, and 500 V endplate offset, *m/z* range from 50 to 3000. The identification of the transformation products was carried out based on MS spectra of precursor ion and the fragmentation pattern with MS/MS. The short-chain carboxylic acids and inorganic ions were analyzed by ionic chromatography (IC) in a Metrohm 790 IC chromatograph, with a Metrosep A Supp column (4 × 250 mm), using Na_2CO_3/$NaHCO_3$ (3.2 mM/1.0 mM) solution as anionic eluent and 100 mM sulfuric acid as anionic suppressor at 0.7 mL min^{-1}. The mineralization degree was measured by means of a total organic carbon (TOC) analyzer (Shimadzu TOC-L device).

3. Results and discussion

3.1. Characterization of the N-cycloalkyl functionalized UiO-66-NH_2 materials

The structure of the newly *N*-cycloalkyl functionalized UiO-66-NH_2 materials was identified and compared with that of the UiO-66-NH_2 pattern by XRD. As shown in Fig. 2, UiO-66-NH_2 and UiO-66-NH-C_5 display the characteristic peaks of the UiO-66-NH_2 pattern [44,45], highlighting the most intense peaks at ca. 7.3 and 8.4° of the (1 1 1) and (2 0 0) Miller planes, which confirm the successful crystallization of the UiO-66-NH_2 framework. The high similarity of both diffractograms indicates the formation of isoreticular structures, as reported previously for the functionalization with the same linkers for MIL-125 [33]. On the contrary, the XRD pattern of the UiO-66-NH-C_6 differs from the UiO-66-NH_2, and only a much wider and less intense peak is observed in the 7–9° region. This result suggests that the use of *N*-cyclohexyl-2-amino terephthalic acid as a linker disfavors the crystallization and results in a structure with low crystallinity and poor definition.

Solid-state NMR has been demonstrated to be a useful tool to unveil the structure of MOFs due to the presence of organic molecules in their structures [46]. Fig. 3 depicts the ^{13}C solid-state NMR spectra of the UiO-66-NH_2 and their *N*-cycloalkyl functionalized derivatives, in which two differenced regions can be observed. The peaks located at high chemical shifts, namely at c.a. 171, 151, 139, 132, and 117 ppm can be ascribed to aromatic carbon nuclei including the carbon nuclei within a carboxylic group or the carbon nuclei attached to the amino group, common to all synthesized materials [47]. Concretely, the signal at 171 ppm was characteristic of C atoms from the carboxylic groups (–COO–, the sum of C_7 and C_8). The C_{ar}–NH_2 group (C_1) appears at ~151 ppm, while the signals at ~139, ~132, ~123, and ~117 ppm can be assigned to the C nuclei of the aromatic ring (C_3, C_5, C_2, and the sum C_4 and C_6, respectively) [48]. In this region of high chemical shifts, a peak located at ca. 163.5 ppm is observed in all the samples which can be described by the existence of carbonyl groups such as in DMF (–N–CHO) occluded in the structure of the MOFs. In the region of low chemical shifts, the *N*-cycloalkyl functionalized samples displayed other new peaks associated with the carbon nuclei of the cycloalkyl rings. Hence, the signals at c.a. 54, 31, and 25 ppm (or 26 + 24 ppm) can be attributed to the carbon nuclei of the cycles linked to the amine group. In this region two peaks associated with DMF were detected, i.e. those located at 31 and 36 ppm, due to the CH_3–N = carbon nuclei of the solvent.

FTIR technique was also carried out to unveil the structure of MOF

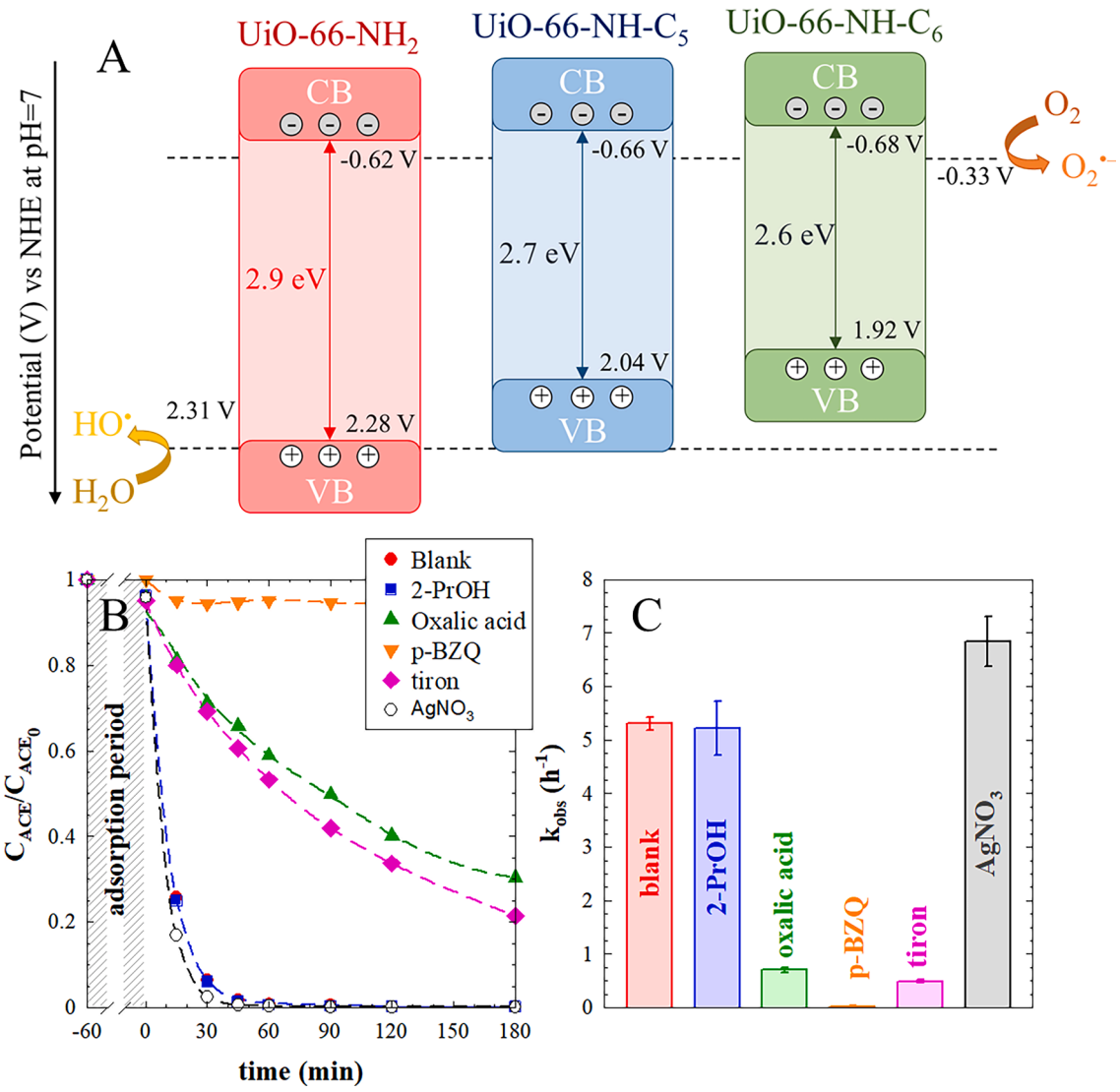

Fig. 9. (A) Proposed bands alignment. (B) Scavengers influence on the time-course normalized concentration of ACE with UiO-66-NH-C_5 and (C) their corresponding pseudo-first order rate constant *($V = 250$ mL; $C_{ACE,0} = 5$ mg L^{-1}, $C_{CAT} = 250$ mg L^{-1}; $T = 25$ °C, $pH_0 = 4.0 \pm 0.2$).*

structure and provide additional evidence of the results observed in the ^{13}C solid-state NMR technique. The FTIR spectra are depicted in Fig. S6, very similar to the registered for the linkers (Fig. S5), with some additional peaks due to the presence of Zr. The wide band at 3400 cm^{-1} can be attributed to the stretching vibration O—H of water molecules physisorbed on the surface or intercrystalline water [49]. The contribution of the υ_{sym}(N–H_2) vibration at 3455 cm^{-1} [50,51] appears to overlap with the previously mentioned O—H stretching. This band was decreased in the *N*-cycloalkylated MOFs. Close to this band, there is a peak at 3355 cm^{-1} assigned to the υ_{asym}(N–H_2) or υ_{asym}(N—H) vibration that appears with barely the same intensity in all the samples. Next, the bands located at ca. 2930 and 2860 cm^{-1} [50] are attributed to the aliphatic stretching of the aliphatic C—H bond [49,52]. It is noteworthy that these peaks are barely observed in the UiO-66-NH_2 sample whereas in the *N*-cycloalkyl modified samples these peaks appear clearly defined as a consequence of the presence of the cycloalkyl rings in the functionalized linker. At 1659 cm^{-1} is observed a peak of the in-plane scissoring bending δ(N–H_2) [50]. Moreover, the three samples exhibited strong vibrational bands at 1386 and 1572 cm^{-1} characteristic of υ_{sym}(O–C═O) and υ_{asym}(O–C═O) stretching due to the presence of carboxylate groups of the terephthalic acid ligand [53]. A less intense peak at ca. 1502 cm^{-1} is attributable to the vibration of the C═C in the aromatic ring [27,53,54]. The stretching of $\upsilon(C_{ar}–N)$ led to the presence of two intense bands at 1386 and 1280 cm^{-1} detected in the three samples [53,55]. Further, in the FTIR spectra, a strong characteristic peak appeared at 765 cm^{-1}, mainly ascribed to a mixture of the O—H and C—H vibrational bindings [49,53,56]. Finally, in the region of lowest frequency values, some peaks related to the $[Zr_6O_4(OH)_4]$ oxocluster were observed, characteristic of the MOF structure and not visible in the FTIR spectra of the linkers, see Fig. S5. The bands at 655, 506, and 482 cm^{-1} were attributed, respectively, to the μ_3–O, Zr(O—C), and μ_3–OH stretching [27,53,57]. In conclusion, FTIR spectra support the results of solid-state NMR, confirming the formation of the MOF structure with the *N*-cycloalkyl functionalized linker.

The SEM pictures displayed in Fig. 4 show different morphology and particle sizes for the different samples. UiO-66-NH_2 shows agglomeration of particles of globular aspect and very small size, an average of 30 nm. The morphology of UiO-66 is reported as well-defined octahedral nanoparticles of an average of 150–200 nm [58]. Although UiO-66-NH_2 can show the octahedral structure of UiO-66 [27,58], it is also frequently observed with a certain deformation of the edges, displaying a morphology closer to a spherical geometry [59,60] and lower particle size [52,58]. An analysis of the particle distribution of UiO-66-NH_2 (see Fig. 4D) led to an average value of 32 nm of particles within 20–55 nm.

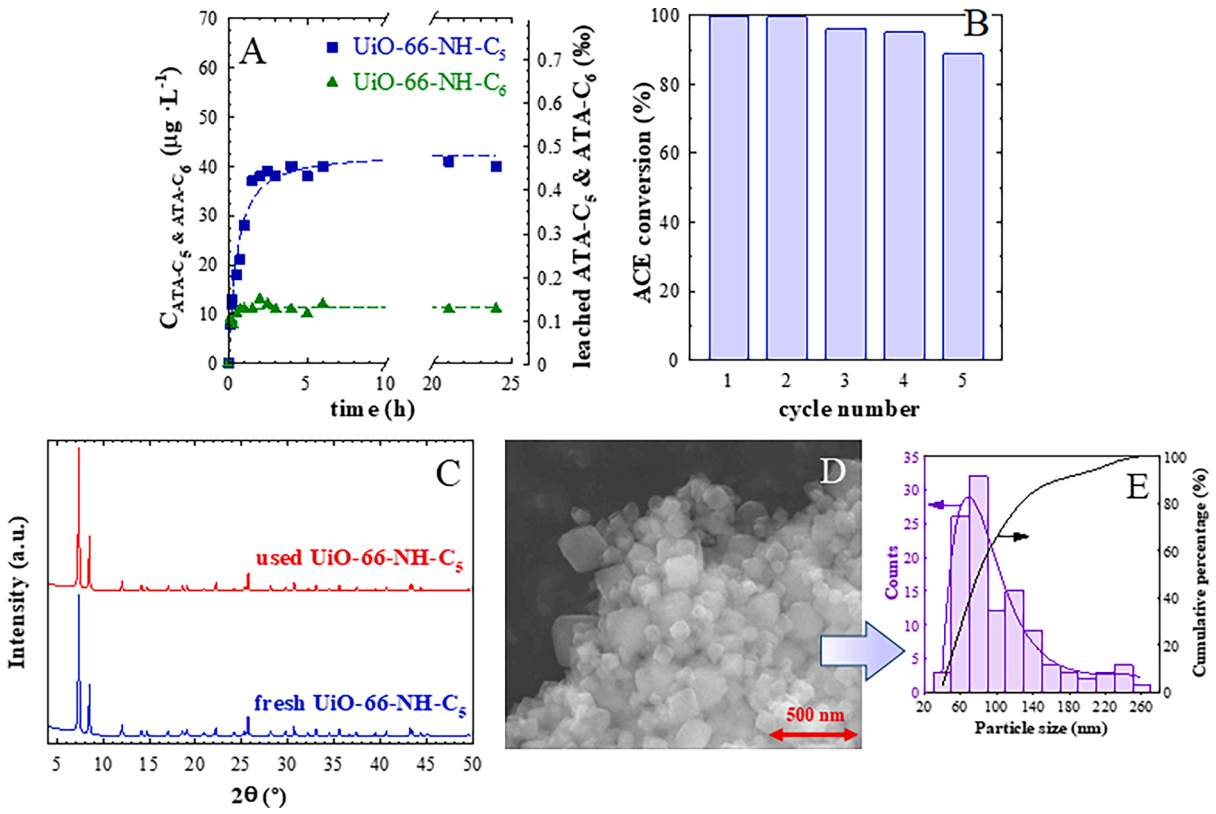

Fig. 10. (A) Linker leaching of UiO-66-NH-C_5 and UiO-66-NH-C_6 *($V = 250$ mL; $C_{ACE,0} = 5$ mg L^{-1}, $C_{CAT} = 250$ mg L^{-1}; $T = 25$ °C, $pH_0 = 4.0 \pm 0.2$)*. (B) ACE photocatalytic conversion with UiO-66-NH-C_5 at 3 h during sequential recycling uses. (C) XRD pattern of UiO-66-NH-C_5 after the 5th reuse cycle. (D) SEM picture of UiO-66-NH-C_5 after the 5th reuse cycle. (E) Particle size distribution of UiO-66-NH_2 after the 5th reuse cycle.

The functionalization of the amino group with a cyclopentyl ring, i.e. UiO-66-NH-C_5, led to a structure consisting of an agglomeration of well-defined cubic-shape particles of uneven sizes within 20–180 nm. Fig. 4E shows the particle size distribution of UiO-66-NH-C_5 in which is possible to observe that most of the particles have a size within the range of 30–80 nm with an overall average size of 67 nm, approximately the double of UiO-66-NH_2. In the case of the UiO-66-NH-C_6, the morphology obtained was irregular, with no definition of particular geometry, and bigger size, i.e. over 1 μm. This lack of ordered morphology agrees well with the poor crystallinity of this sample observed in the XRD patterns (Fig. 2).

Fig. 5 represents the N_2 adsorption–desorption isotherms and Table 1 summarizes the characteristic parameters of the porous texture. According to IUPAC classification, the isotherms describe a Type II isotherm for UiO-66-NH_2 and UiO-66-NH-C_5, whereas UiO-66-NH-C_6 follows a Type I profile. All of them are characteristic of highly microporous materials. The hysteresis loop registered for UiO-66-NH_2 and UiO-66-NH-C_5 provides evidence of a certain contribution of mesoporosity. The specific BET surface areas (Table 1) decreased with increasing the volume of the *N*-cycloalkyl substitution, i.e. the areas follow the order UiO-66-NH_2 > UiO-66-NH-C_5 > UiO-66-NH-C_6. This behavior was also observed when analyzing the pore volumes. On account of the pore size distribution (Fig. 5 inlet), most of the micropores of both *N*-cycloalkyl functionalized samples were located within 1.0–1.5 nm, with a maximum located at around 1.1 nm. However, UiO-66-NH_2 displayed a great number of micropores of lower size, i.e. 0.8 nm, with minor contributions of micropores with sizes between 1.1 and 1.5 nm. These results suggest that the addition of extra substituents, such as *N*-cycloalkyl, diminishes the accessibility to the pores due to the clogging of the pore and their apertures, as also reported in the literature for MIL-125 after functionalization in the amino group [33]. However, regarding the proportion of micropores (V_{MP}/V_T), the tuning with *N*-cycloalkyl increases the micropore ratio due to the mentioned clogging effect. Therefore, the functionalization seems to reduce the average pore size of the resulting MOF.

Fig. 6A displays the UV–vis absorption profiles. UiO-66-NH_2 shows two distinctive absorption bands. The band located at 250 nm is ascribed to transferences of electrons from O to Zr centers in the $[Zr_6O_4(OH)_4]$ metal oxocluster [60]. The band whose maximum was placed at 385 nm, is a consequence of the π-π electron transitions from the NH_2–based chromophores of the linker to the $[Zr_6O_4(OH)_4]$ cluster [61]. The *N*-cycloalkyl functionalized samples maintain similar absorption profiles to that of UiO-66-NH_2 in the UV region, with the same abovementioned bands although with lower intensities. Furthermore, the *N*-cycloalkyl-2-aminoterephtalate linkers generated red-shifted spectra, due to the presence of the alkyl donor group which is thought to destabilize the energy of the 2-aminoterephthalate [33]. This results in inductive electron effects of the *N*-cycloalkyl chain in the amino group, with strong σ-bonds in its proximity [33], decreasing the bandgap energy. The Tauc plot (Fig. 6B) shows a decrease in the bandgap values (Table 2) by using *N*-cycloalkyl-2-aminoterephtalatic linkers, following the order: UiO-66-NH_2 > UiO-66-NH-C_5 > UiO-66-NH-C_6.

3.2. Photocatalytic activity of the N-cycloalkyl-amino UiO-66-NH_2 photocatalysts

The photocatalytic activity was tested in the degradation of ACE in water. Since MOFs are porous structures with a potential ability for adsorption of organics in an aqueous solution [62,63], a 1-hour adsorption step was carried out before the photocatalytic step. Fig. 7A represents the temporal evolution of the normalized concentration of ACE during the photocatalytic degradation, while Fig. 7B depicts the calculated pseudo-first order rate constants. ACE adsorption was almost negligible in the three samples, in agreement with the previously

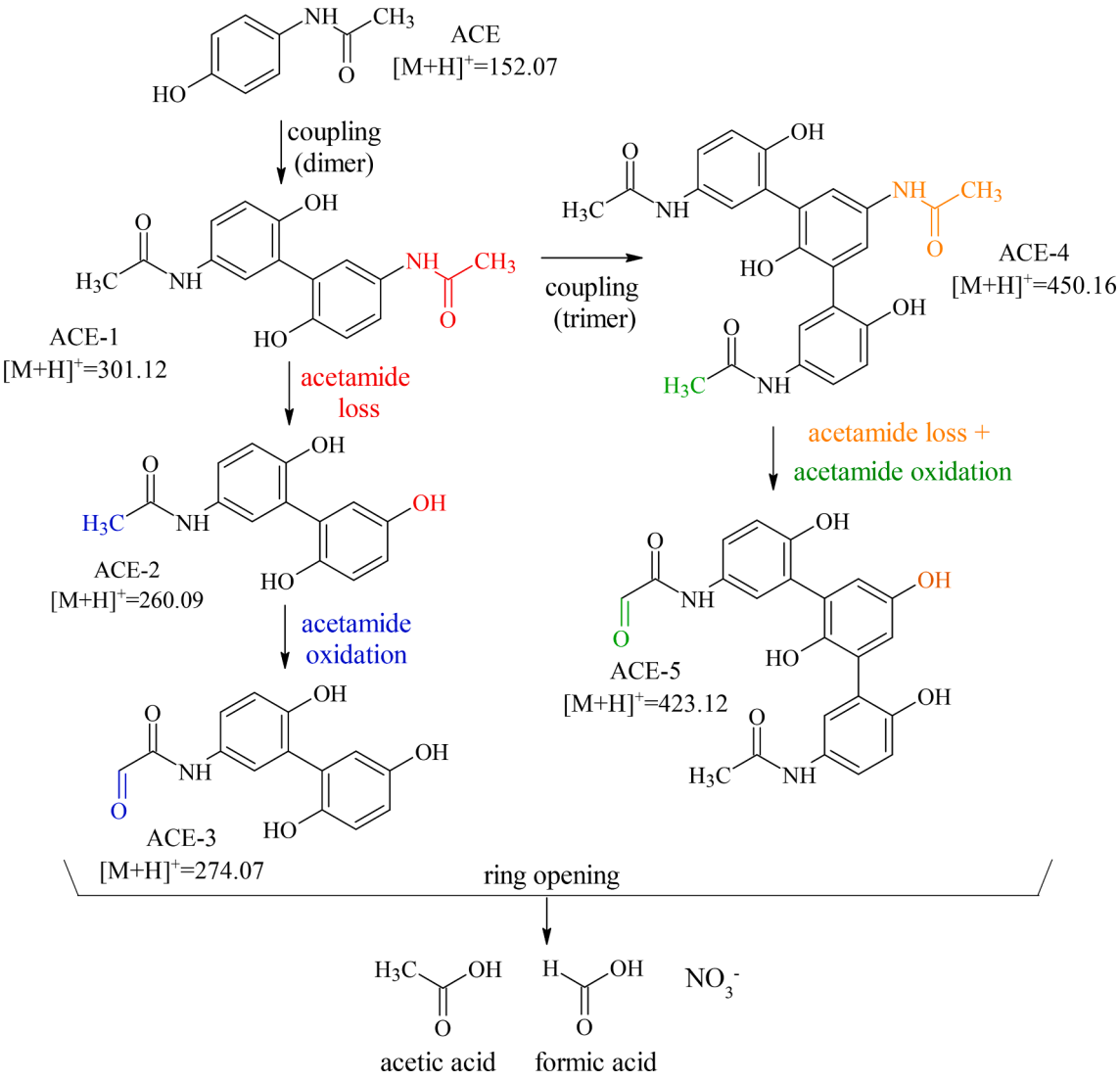

Fig. 11. Proposed photocatalytic degradation pathway of ACE with UiO-66-NH-C_5.

reported for UiO-66 and UiO-66-NH_2 [27]. It is also remarkable the high stability of ACE under irradiation in the absence of photocatalysts (photolysis). In the presence of UiO-66-NH_2, the ACE was completely degraded in 4 h with a pseudo-first order rate constant equal to 0.82 h^{-1}. This value is consistent with the reported values in the literature. For example, Wang et al. [27] obtained a pseudo-first order rate constant of 0.37 h^{-1} for the degradation of ACE with UiO-66-NH_2 under similar experimental conditions. The functionalization of the amino group with cycloalkyl rings led to a considerable improvement in the kinetics of ACE degradation. As compared in Fig. 7B, UiO-66-NH-C_5 achieved a ~5.5 times higher value of the kinetic constant than UiO-66-NH_2, reaching ACE complete degradation after only 1 h of irradiation. The functionalization with the cyclohexane ring also improved the UiO-66-NH_2 results, but to a lesser extent.

UiO-66-NH-C_5 displayed the best photo-activity results, but this is difficult to justify based on the crystal, textural and optical properties. To further explore the photocatalytic activity of UiO-66-NH-C_5 based on charge mobility, electrochemical impedance spectroscopy (EIS) was applied [64]. This technique analyzes the resistance to the charge transfer monitored on the surface of the MOF. Fig. 8 depicts the Nyquist curves in which the radius of the described semicircles follows the order UiO-66-NH_2 < UiO-66-NH-C_6 < UiO-66-NH-C_5. Since the diameters of the semicircles are equal to the electrical resistance of a sample, the smaller arc radius reflects a lower resistance suggesting, therefore, a decrease in the solid-state interface layer resistance and the charge transfer resistance across the solid–liquid junction on the surface [65–67]. The electrical transfer resistance followed the order UiO-66-NH_2 < UiO-66-NH-C_6 < UiO-66-NH-C_5, in agreement with the inverse order of the photoactivity or degradation reaction rates. This suggests that the best results obtained with UiO-66-NH-C_5 can be justified by the lower charge transfer resistance and thus, the better mobility of charges in this sample.

3.3. Elucidation of the photocatalytic degradation mechanism

The scheme of the band energy alignments of bare and *N*-cycloalkyl functionalized photocatalysts is proposed in Fig. 9A. For that, the potential of the valence and conduction bands were previously estimated from the flat band potential calculated via electrochemical trough Mott-Schottky measurements (see Fig. S7) and the bandgap energy. The flat band potential of the sample UiO-66-NH_2 was calculated from the Mott-Schottky plot, i.e. –0.80 V (NHE scale at pH = 7). This value is similar to the values reported in the literature for this MOF [59,60,68,69]. The presence of *N*-cycloalkyl groups does not change the flat band value, and the redox potential of the conduction band was quite similar (see Table 2). The V_{CB} value obtained in all synthesized samples is more negative than the redox potential of the pair $O_2/O_2^{\bullet-}$, i.e. −0.33 V vs NHE at pH = 7 [70]. Therefore, the formation of the superoxide is

thermodynamically feasible according to the proposed band alignment schemes. Nonetheless, the formation of hydroxyl radicals is not energetically plausible since the redox potential of the photogenerated holes is lower in all the cases than the value needed for the water molecule oxidation, i.e·$H_2O/HO^{\bullet}$, +2.31 V vs NHE at pH = 7 [71].

Scavenger tests were taken to tentatively elucidate the reactive oxidant species involved in the photocatalytic degradation process of ACE with the UiO-66-NH-C_5. Fig. 9B displays the scavenger influence on the evolution of ACE concentration during photocatalytic degradation with UiO-66-NH-C_5 and Fig. 9C the corresponding pseudo-first order rate constants. The influence of $HO^{\bullet}$ was firstly assessed by a probe method monitoring the formation of the highly fluorescent 2-OH-TA from the selective reaction of $HO^{\bullet}$ and TA [41–43]. Fig. S8 depicts the time-course of 2-OH-TA concentration, and a maximum concentration of 24 μM is observed. However, the amount of $HO^{\bullet}$ in the solution seems to be insufficient for the ACE degradation. This fact was observed using 2-PrOH as scavenger. 2-PrOH is used as a $HO^{\bullet}$ scavenger due to the high rate constant of the reaction between this alcohol and $HO^{\bullet}$, i.e. 2×10^9 M^{-1} s^{-1} [72]. The addition of 2-PrOH did not alter the kinetics of the ACE degradation, which pointed out the lack of influence of $HO^{\bullet}$ in the process, as suggested by the band alignments proposal. The contribution of the holes was suppressed in the presence of oxalic acid (10 mM) which is oxidized by holes to produce CO_2 [73]. The addition of oxalic acid slowed down the ACE abatement, reducing the pseudo-first order rate constant at the beginning of the process by over 7 times, which evidences the importance of the h^+ in the ACE degradation. For the suppression of the possible superoxide contribution, *p*-benzoquinone (*p*-BZQ) is frequently used due to the high rate constant among them, i.e. (0.9–1) 10^9 M^{-1} s^{-1} [74,75]. The results obtained of ACE abatement in the presence of p-BZQ displayed a great inhibition effect. However, as the selectivity of p-BZQ towards superoxide radical is not complete [73], an alternative superoxide scavenger such as tiron was also tested. Tiron reacts with superoxide radicals with a high rate constant, i.e. 5×10^8 M^{-1} s^{-1} [76], and also with $HO^{\bullet}$, whose contribution has been previously neglected. The addition of tiron (1 mM) led to almost 11 times decreased k_{obs} for ACE degradation if compared to the blank test. This fact manifests that superoxide radical contributes to ACE degradation. Finally, Ag^+ cation was used for testing the importance of photogenerated electrons. In the presence of $AgNO_3$, a slight acceleration, 30 % increased k_{obs}, was appreciated due to the reduction of the electron-hole recombination rate as the photo-generated electrons are consumed during the Ag^+ reduction [59,77].

3.4. Stability in water and reusability

One of the most critical aspects of MOFs applications is their stability in water [78]. Water molecules can induce the collapse of certain MOF structures because the adsorption–desorption of these H_2O molecules can easily induce a vibration of the ligands, which can favor the breakage of the bonds with the metallic cluster eventually collapse the whole structure [79]. The stability of the UiO-66 family has been assessed by the analysis of the possible leached metal or linker into water. For instance, the release of Zr^{4+} by UiO-66 in water has been reported undetectable, except under extreme concentrations of buffer in which the structure tends to collapse [80]. Besides, UiO-66-NH_2 displays very high stability in water with almost negligible lixiviation of ATA in a wide range of pH ranges [59]. On this basis, the stability of the *N*-cycloalkyl functionalized UiO-66-NH_2 materials reported in this work was analyzed by the quantification of the linker lixiviation, i.e. ATA-C_5 and ATA-C_6, for 24 h at natural pH. As shown in Fig. 10A, the lixiviation of ATA-C_5 from UiO-66-NH-C_5 and ATA-C_6 from UiO-NH-C_6 are minimal and in the range of μg L^{-1}. Considering the percentage of the leached linker concerning the linker constituting the MOF structure [59], only 0.44 ‰ of ATA-C_5 and 0.13 ‰ of ATA-C_6 are detected, values following the 0.20 ‰ already reported for UiO-66-NH_2 [59].

Based on the photocatalytic performance, UiO-66-NH-C_5 was selected for a study of photocatalytic activity with sequential reusing cycles. Fig. 10B shows the ACE conversion at 3 h of treatment during 5 consecutive cycles of reuse. UiO-66-NH-C_5 performs a very stable activity with a slight loss in the last run, less than 10 %, attributable to the catalyst loss during recuperation between runs. The stability of the functionalized MOF was also tested in terms of structural properties. Fig. 10C depicts the XRD pattern of UiO-66-NH-C_5 after being reused five times. As can be observed, no differences in the crystalline structure were achieved, which provides evidence of the stability of UiO-66-NH-C_5. Furthermore, SEM imaging (Fig. 10D) confirmed the lack of geometrical deformation of the cubic-shape particles. Moreover, the profile of the particle size distribution after use was quite similar to the fresh sample (see Fig. 10E).

3.5. Photocatalytic degradation pathway of acetaminophen

The transformation products produced during the photocatalytic abatement of ACE were tentatively identified by liquid chromatography coupled to electrospray ionization-mass spectrometry, at an ACE initial concentration of 100 mg L^{-1} using the most photoactive MOF sample, UiO-66-NH-C_5. The proposed transformation products and the properties obtained during their identification are enlisted in Table S1 and the suggested degradation pathway is depicted in Fig. 11. The direct oxidation of ACE by hydroxylation is usually expected if the $HO^{\bullet}$ is the main oxidant species in the process [81], leading to the oxidation either of the aromatic ring or the attack on the amino alkyl chain of ACE. In the oxidation of ACE over UiO-66-NH-C_5, in which the oxidation of H_2O to $HO^{\bullet}$ has been discarded, this route was not observed. Instead, the photogenerated holes led to a coupling pathway of ACE molecules to produce dimer and trimer forms, as has been reported in the literature. It is thought that a radical coupling of ACE molecules, is induced by the h^+ through one electron oxidation of ACE [81]. As the importance of the photogenerated holes has been previously demonstrated, the photocatalytic abatement of ACE likely involves the initial formation of dimer and trimer species.

Two dimer isomers from the coupling of ACE were detected, ACE-1, as previously reported in the photodegradation of this compound over TiO_2 [81,82] or UiO-66-NH_2 [27]. Two transformation routes of ACE-1 were observed. Firstly, the loss of one of the acetamide groups in ACE-1 led to the namely ACE-2. The ACE-2 launched was oxidized in the *N*-amino methyl chain to launch the formation of the corresponding aldehyde, ACE-3. The second route of ACE-1 reaction was the further coupling with another ACE molecule, leading to the trimer ACE-4. Also, the simultaneous loss and oxidation in two acetamide groups of ACE-4, trigger the formation of ACE-5. The further degradation of these intermediates was indirectly monitored by TOC analysis. The evolution of TOC (Fig. S9A) displayed a 50 % of mineralization after 3 h of reaction which suggested that the transformation products of ACE were successfully degraded. Also, the release of short organic acids, i.e. formic and acetic acids, was observed (Fig. S9B) which provides further evidence of the oxidation ability of the system.

4. Conclusions

This work is an example of the versatility and huge opportunities that MOFs can supply by modifying the linker structure. In this work, *N*-cycloalkyl modified linkers were first prepared and used to build different UiO-66-NH_2 MOFs. Thus, novel isoreticular UiO-66-NH_2 frameworks were successfully prepared with *N*-cyclopentyl and *N*-cyclohexyl 2-amino-terephthalate linkers for the first time. The functionalization of the linker led to a decrease in the bandgap energy and improved the migration of the photo-generated charges. Although the bandgap followed the order UiO-66-NH_2 > UiO-66-NH-C_5 > UiO-66-NH-C_6, the sample UiO-66-NH-C_5 displayed better crystallization and less electrical resistance, therefore, better mobility of charges. These optoelectronic differences explained the outstanding photocatalytic

activity in the acetaminophen removal in water. The determination of the conduction band energy, and the proposal of bands alignment, discharged the plausible role paid by the hydroxyl radicals, confirmed by the scavenger test. Instead, the main role of both photogenerated holes and superoxide radicals was confirmed. Both *N*-cycloalkyl modified UiO-66-NH_2 MOFs were very stable in water with almost no detectable linker leaching, i.e. lower than 0.5 ‰, and the UiO-66-NH-C_5 displayed a high photocatalytic activity during sequential reusing cycles. The identified transformation products were the results of a coupling route in which dimers and trimers of acetaminophen were formed to be further oxidized, as confirmed by the formation of organic acids of low molecular weight, i.e formic and acetic acid, and the evolution of the mineralization degree.

Declaration of Competing Interest

The authors declare the following financial interests/personal relationships which may be considered as potential competing interests: Carolina Belver has patent #EP22382704 pending to Universidad Autónoma de Madrid.

Data availability

Data will be made available on request.

Acknowledgments

This research was funded by the Spanish State Research Agency (PID2019-106186RB-I00/AEI/10.13039/501100011033 and PID2019-105479RB-I00 MCIN/AEI/10.13039/501100011033). Rafael R. Solís thanks the Spanish Ministry of Science, Innovation, and Universities for his postdoctoral contract (*Juan de la Cierva Formación*, Ref. FJC2018-035513-I). The authors also thank the support provided by the external services of the Autonomous University of Madrid (SIdI) and the University of Extremadura (SAIUEx). Funding for open access charge: Universidad de Granada/CBUA.

Appendix A. Supplementary data

Supplementary data to this article can be found online at https://doi.org/10.1016/j.cej.2023.141889.

References

[1] J. Gascon, A. Corma, F. Kapteijn, F.X. Llabrés, I. Xamena, Metal organic framework catalysis: quo vadis? ACS Catal. 4 (2014) 361–378, https://doi.org/10.1021/cs400959k.

[2] J. Bedia, V. Muelas-Ramos, M. Peñas-Garzón, A. Gómez-Avilés, J.J. Rodríguez, C. Belver, A review on the synthesis and characterization of metal organic frameworks for photocatalytic water purification, Catalysts 9 (2019) 52, https://doi.org/10.3390/catal9010052.

[3] N.L. Rosi, J. Eckert, M. Eddaoudi, D.T. Vodak, J. Kim, M. O'Keeffe, O.M. Yaghi, Hydrogen storage in microporous metal-organic frameworks, Science 300 (2003) (1979) 1127–1129, https://doi.org/10.1126/SCIENCE.108344.

[4] S.P. Shet, S. Shanmuga Priya, K. Sudhakar, M. Tahir, A review on current trends in potential use of metal-organic framework for hydrogen storage, Int. J. Hydrogen Energy 46 (2021) 11782–11803, https://doi.org/10.1016/J.IJHYDENE.2021.01.020.

[5] M. Usman, A. Helal, M.M. Abdelnaby, A.M. Alloush, M. Zeama, Z.H. Yamani, Trends and prospects in UiO-66 metal-organic framework for CO_2 capture, separation, and conversion, Chem. Rec. 21 (2021) 1771–1791, https://doi.org/10.1002/TCR.202100030.

[6] Q. Qian, P.A. Asinger, M.J. Lee, G. Han, K. Mizrahi Rodriguez, S. Lin, F. M. Benedetti, A.X. Wu, W.S. Chi, Z.P. Smith, MOF-based membranes for gas separations, Chem. Rev. 120 (2020) 8161–8266, https://doi.org/10.1021/ACS.CHEMREV.0C00119.

[7] E. Adatoz, A.K. Avci, S. Keskin, Opportunities and challenges of MOF-based membranes in gas separations, Sep. Purif. Technol. 152 (2015) 207–237, https://doi.org/10.1016/J.SEPPUR.2015.08.020.

[8] F. Ahmadijokani, H. Molavi, M. Rezakazemi, S. Tajahmadi, A. Bahi, F. Ko, T. M. Aminabhavi, J.R. Li, M. Arjmand, UiO-66 metal–organic frameworks in water treatment: A critical review, Prog. Mater Sci. 125 (2022), 100904, https://doi.org/10.1016/J.PMATSCI.2021.100904.

[9] D. Yang, B.C. Gates, Catalysis by metal organic frameworks: perspective and suggestions for future research, ACS Catal. 9 (2019) 1779–1798, https://doi.org/10.1021/ACSCATAL.8B04515.

[10] D. Li, H.Q. Xu, L. Jiao, H.L. Jiang, Metal-organic frameworks for catalysis: state of the art, challenges, and opportunities, EnergyChem 1 (2019), 100005, https://doi.org/10.1016/J.ENCHEM.2019.100005.

[11] M.A. Tahir, N. Arshad, M. Akram, Recent advances in metal organic framework (MOF) as electrode material for super capacitor: A mini review, J. Energy Storage 47 (2022), 103530, https://doi.org/10.1016/J.EST.2021.103530.

[12] S. Dong, L. Wu, M. Xue, Z. Li, D. Xiao, C. Xu, L. Shen, X. Zhang, Conductive metal-organic framework for high energy sodium-ion hybrid capacitors, ACS Appl. Energy Mater. 4 (2021) 1568–1574, https://doi.org/10.1021/ACSAEM.0C02758.

[13] H.D. Lawson, S.P. Walton, C. Chan, Metal-organic frameworks for drug delivery: a design perspective, ACS Appl. Mater. Interfaces 13 (2021) 7004–7020, https://doi.org/10.1021/ACSAMI.1C01089.

[14] W. Duan, Z. Zhao, H. An, Z. Zhang, P. Cheng, Y. Chen, H. Huang, State-of-the-art and prospects of biomolecules: incorporation in functional metal–organic frameworks, in: X.H. Bu, M. Zaworotko, Z. Zhang (Eds.), Metal-Organic Framework. Topics in Current Chemistry Collections, Springer International Publishing, 2020, pp. 57–87, https://doi.org/10.1007/978-3-030-47340-2_2.

[15] Y. Sun, L. Zheng, Y. Yang, X. Qian, T. Fu, X. Li, Z. Yang, H. Yan, C. Cui, W. Tan, Metal–organic framework nanocarriers for drug delivery in biomedical applications, Nano-Micro Lett. 12 (2020) 1–29. doi:10.1007/S40820-020-00423-3.

[16] P. Tong, J. Liang, X. Jiang, J. Li, Research progress on metal-organic framework composites in chemical sensors, Crit. Rev. Anal. Chem. 50 (2019) 376–392, https://doi.org/10.1080/10408347.2019.1642732.

[17] L.E. Kreno, K. Leong, O.K. Farha, M. Allendorf, R.P. Van Duyne, J.T. Hupp, Metal–organic framework materials as chemical sensors, Chem. Rev. 112 (2011) 1105–1125, https://doi.org/10.1021/CR200324T.

[18] T. Zhang, W. Lin, Metal–organic frameworks for artificial photosynthesis and photocatalysis, Chem. Soc. Rev. 43 (2014) 5982–5993, https://doi.org/10.1039/C4CS00103F.

[19] M. Alvaro, E. Carbonell, B. Ferrer, F. LlabrésiXamena, H. Garcia, Semiconductor behavior of a metal-organic framework (MOF), Chem. A Eur. J. 13 (18) (2007) 5106–5112, https://doi.org/10.1002/chem.200601003.

[20] W. Ni, A. Khan, Modified metal-organic frameworks as photocatalysts, in: Metal-Organic Frameworks for Chemical Reactions, Elsevier, 2021: pp. 231–270. doi:10.1016/B978-0-12-822099-3.00010-1.

[21] J. Joseph, S. Iftekhar, V. Srivastava, Z. Fallah, E.N. Zare, M. Sillanpää, Iron-based metal-organic framework: Synthesis, structure and current technologies for water reclamation with deep insight into framework integrity, Chemosphere 284 (2021), 131171, https://doi.org/10.1016/J.CHEMOSPHERE.2021.131171.

[22] X. Zhang, S. Tong, D. Huang, Z. Liu, B. Shao, Q. Liang, T. Wu, Y. Pan, J. Huang, Y. Liu, M. Cheng, M. Chen, Recent advances of Zr based metal organic frameworks photocatalysis: Energy production and environmental remediation, Coord. Chem. Rev. 448 (2021), 214177, https://doi.org/10.1016/J.CCR.2021.214177.

[23] L. Li, X.S. Wang, T.F. Liu, J. Ye, Titanium-based MOF materials: from crystal engineering to photocatalysis, Small Methods 4 (2020) 2000486, https://doi.org/10.1002/SMTD.202000486.

[24] H. Dai, X. Yuan, L. Jiang, H. Wang, J. Zhang, J. Zhang, T. Xiong, Recent advances on ZIF-8 composites for adsorption and photocatalytic wastewater pollutant removal: Fabrication, applications and perspective, Coord. Chem. Rev. 441 (2021), 213985, https://doi.org/10.1016/J.CCR.2021.213985.

[25] J.H. Cavka, S. Jakobsen, U. Olsbye, N. Guillou, C. Lamberti, S. Bordiga, K. P. Lillerud, A new zirconium inorganic building brick forming metal organic frameworks with exceptional stability, J. Am. Chem. Soc. 130 (42) (2008) 13850–13851, https://doi.org/10.1021/ja8057953.

[26] J. Winarta, B. Shan, S.M. Mcintyre, L. Ye, C. Wang, J. Liu, B. Mu, A decade of UiO-66 research: A historic review of dynamic structure, synthesis mechanisms, and characterization techniques of an archetypal metal−organic framework, Cryst. Growth Des. 20 (2020) 1347–1362, https://doi.org/10.1021/acs.cgd.9b00955.

[27] Y.L. Wang, S. Zhanb, Y.F. Zhab, J. Bedia, J.J. Rodriguez, C. Belver, UiO-66 based metal organic frameworks for the photodegradation of acetaminophen under simulated solar irradiation, J. Environ. Chem. Eng. 9 (2021), 106087, https://doi.org/10.1016/j.jece.2021.106087.

[28] X. Mu, J. Jiang, F. Chao, Y. Lou, J. Chen, Ligand modification of UiO-66 with an unusual visible light photocatalytic behavior for RhB degradation, Dalton Trans. 47 (2018) 1895–1902, https://doi.org/10.1039/C7DT04477A.

[29] T.F. Chen, S.Y. Han, Z.P. Wang, H. Gao, L.Y. Wang, Y.H. Deng, C.Q. Wan, Y. Tian, Q. Wang, G. Wang, G.S. Li, Modified UiO-66 frameworks with methylthio, thiol and sulfonic acid function groups: The structure and visible-light-driven photocatalytic property study, Appl. Catal. B 259 (2019), 118047, https://doi.org/10.1016/J.APCATB.2019.118047.

[30] X. Chen, Y. Cai, R. Liang, Y. Tao, W. Wang, J. Zhao, X. Chen, H. Li, D. Zhang, NH_2-UiO-66(Zr) with fast electron transfer routes for breaking down nitric oxide via photocatalysis, Appl. Catal. B 267 (2020), 118687, https://doi.org/10.1016/j.apcatb.2020.118687.

[31] T. Musho, J. Li, N. Wu, Band gap modulation of functionalized metal–organic frameworks, PCCP 16 (2014) 23646–23653, https://doi.org/10.1039/C4CP03110E.

[32] J. Li, T. Musho, J. Bright, N. Wu, Functionalization of a metal-organic framework semiconductor for tuned band structure and catalytic activity, J. Electrochem. Soc. 166 (2019) H3029–H3034. doi:10.1149/2.0051905JES/XML.

[33] M.W. Logan, S. Ayad, J.D. Adamson, T. Dilbeck, K. Hanson, F.J. Uribe-Romo, Systematic variation of the optical bandgap in titanium based isoreticular metal-organic frameworks for photocatalytic reduction of CO_2 under blue light, J. Mater. Chem. A Mater. 5 (2017) 11854–11863, https://doi.org/10.1039/c7ta00437k.

[34] C.B. v. Muelas-Ramos, M. Peñas-Garzón, J.J. Rodriguez, J. Bedia, Solar photocatalytic degradation of emerging contaminants using NH_2-MIL-125 grafted by heterocycles, Sep. Purif. Technol. 297 (2022) 121442. doi:10.1016/j.seppur.2022.121442.

[35] X. Yang, R.C. Flowers, H.S. Weinberg, P.C. Singer, Occurrence and removal of pharmaceuticals and personal care products (PPCPs) in an advanced wastewater reclamation plant, Water Res. 45 (2011) 5218–5228, https://doi.org/10.1016/J.WATRES.2011.07.026.

[36] A. Pal, K.-Y.-H. Gin, A.-Y.-C. Lin, M. Reinhard, Impacts of emerging organic contaminants on freshwater resources: Review of recent occurrences, sources, fate and effects, Sci. Total Environ. 408 (2010) 6062–6069, https://doi.org/10.1016/J.SCITOTENV.2010.09.026.

[37] P. Makuła, M. Pacia, W. Macyk, How to correctly determine the band gap energy of modified semiconductor photocatalysts based on UV-vis spectra, J. Phys. Chem. Lett. 9 (2018) 6814–6817, https://doi.org/10.1021/acs.jpclett.8b02892.

[38] M. Zeama, M. Morsy, S. Abdel-Azeim, M. Abdelnaby, A. Alloush, Z. Yamani, Photophysical and photocatalytic properties of structurally modified UiO-66, Inorgan. Chim. Acta 501 (2020), 119287, https://doi.org/10.1016/J.ICA.2019.119287.

[39] K. Gelderman, L. Lee, S.W. Donne, Flat-band potential of a semiconductor: Using the Mott-Schottky equation, J. Chem. Educ. 84 (2007) 25, https://doi.org/10.1021/ed084p685.

[40] T. Giannakopoulou, I. Papailias, N. Todorova, N. Boukos, Y. Liu, J. Yu, C. Trapalis, Tailoring the energy band gap and edges' potentials of g-C_3N_4/TiO_2 composite photocatalysts for NO_x removal, Chem. Eng. J. 310 (2017) 571–580, https://doi.org/10.1016/J.CEJ.2015.12.102.

[41] W.H.M. Abdelraheem, M.K. Patil, M.N. Nadagouda, D.D. Dionysiou, Hydrothermal synthesis of photoactive nitrogen- and boron- codoped TiO_2 nanoparticles for the treatment of bisphenol A in wastewater: Synthesis, photocatalytic activity, degradation byproducts and reaction pathways, Appl. Catal. B 241 (2019) 598–611, https://doi.org/10.1016/J.APCATB.2018.09.039.

[42] S. Gligorovski, R. Strekowski, S. Barbati, D. Vione, Environmental implications of hydroxyl radicals ($^{\bullet}OH$), Chem. Rev. 115 (2015) 13051–13092, https://doi.org/10.1021/CR500310B.

[43] M. Sahni, B.R. Locke, Quantification of hydroxyl radicals produced in aqueous phase pulsed electrical discharge reactors, Ind. Eng. Chem. Res. 45 (2006) 5819–5825, https://doi.org/10.1021/IE0601504.

[44] R.M. Cedeno, R. Cedeno, M.A. Gapol, T. Lerdwiriyanupap, S. Impeng, A. Flood, S. Bureekaew, Bandgap modulation in Zr-based metal-organic frameworks by mixed-linker approach, Inorg. Chem. 60 (2021) 8908–8916, https://doi.org/10.1021/ACS.INORGCHEM.1C00792.

[45] Y. Zhang, T. Dai, F. Zhang, J. Zhang, G. Chu, C. Quan, Fe_3O_4@UiO-66-NH_2 core–shell nanohybrid as stable heterogeneous catalyst for Knoevenagel condensation, Chin. J. Catal. 37 (2016) 2106–2113, https://doi.org/10.1016/S1872-2067(16)62562-7.

[46] B.E.G. Lucier, S. Chen, Y. Huang, Characterization of metal–organic frameworks: Unlocking the potential of solid-state NMR, Acc. Chem. Res. 51 (2017) 319–330, https://doi.org/10.1021/ACS.ACCOUNTS.7B00357.

[47] E. Žunkovič, M. Mazaj, G. Mali, M. Rangus, T. Devic, C. Serre, N. Zabukovec Logar, Structural study of Ni- or Mg-based complexes incorporated within UiO-66-NH_2 framework and their impact on hydrogen sorption properties, J. Solid State Chem. 225 (2015) 209–215. doi:10.1016/J.JSSC.2014.12.033.

[48] S. Devautour-Vinot, G. Maurin, C. Serre, P. Horcajada, D. Paula Da Cunha, V. Guillerm, E. De Souza Costa, F. Taulelle, C. Martineau, Structure and dynamics of the functionalized MOF type UiO-66(Zr): NMR and dielectric relaxation spectroscopies coupled with DFT calculations, Chem. Mater. 24 (2012) 2168–2177, https://doi.org/10.1021/CM300863C.

[49] L. Valenzano, B. Civalleri, S. Chavan, S. Bordiga, M.H. Nilsen, S. Jakobsen, K. P. Lillerud, C. Lamberti, Disclosing the complex structure of UiO-66 metal organic framework: A synergic combination of experiment and theory, Chem. Mater. 23 (2011) 1700–1718, https://doi.org/10.1021/cm1022882.

[50] M. Kandiah, S. Usseglio, S. Svelle, U. Olsbye, K.P. Lillerud, M. Tilset, Post-synthetic modification of the metal–organic framework compound UiO-66, J. Mater. Chem. 20 (2010) 9848–9851, https://doi.org/10.1039/C0JM02416C.

[51] H. Saleem, U. Rafique, R.P. Davies, Investigations on post-synthetically modified UiO-66-NH_2 for the adsorptive removal of heavy metal ions from aqueous solution, Micropor. Mesopor. Mater. 221 (2016) 238–244, https://doi.org/10.1016/J.MICROMESO.2015.09.043.

[52] K. Chakarova, I. Strauss, M. Mihaylov, N. Drenchev, K. Hadjiivanov, Evolution of acid and basic sites in UiO-66 and UiO-66-NH_2 metal-organic frameworks: FTIR study by probe molecules, Micropor. Mesopor. Mater. 281 (2019) 110–122, https://doi.org/10.1016/J.MICROMESO.2019.03.006.

[53] G.Y. Shangkum, P. Chammingkwan, D.X. Trinh, T. Taniike, Design of a semi-continuous selective layer based on deposition of UiO-66 nanoparticles for nanofiltration, Membranes (Basel) 8 (2018) 129, https://doi.org/10.3390/MEMBRANES8040129.

[54] J.B. Decoste, G.W. Peterson, H. Jasuja, T.G. Glover, Y.G. Huang, K.S. Walton, Stability and degradation mechanisms of metal–organic frameworks containing the $Zr_6O_4(OH)_4$ secondary building unit, J. Mater. Chem. A Mater. 1 (2013) 5642–5650, https://doi.org/10.1039/C3TA10662D.

[55] K. Vellingiri, A. Deep, K.H. Kim, D.W. Boukhvalov, P. Kumar, Q. Yao, The sensitive detection of formaldehyde in aqueous media using zirconium-based metal organic frameworks, Sens. Actuators B Chem. 241 (2017) 938–948, https://doi.org/10.1016/J.SNB.2016.11.017.

[56] M. Kandiah, M.H. Nilsen, S. Usseglio, S. Jakobsen, U. Olsbye, M. Tilset, C. Larabi, E.A. Quadrelli, F. Bonino, K.P. Lillerud, Synthesis and stability of tagged UiO-66 Zr-MOFs, Chem. Mater. 22 (2010) 6632–6640, https://doi.org/10.1021/CM102601V.

[57] J. Ding, Z. Yang, C. He, X. Tong, Y. Li, X. Niu, H. Zhang, UiO-66(Zr) coupled with Bi_2MoO_6 as photocatalyst for visible-light promoted dye degradation, J. Colloid Interface Sci. 497 (2017) 126–133, https://doi.org/10.1016/J.JCIS.2017.02.060.

[58] W. Zhao, T. Ding, Y. Wang, M. Wu, W. Jin, Y. Tian, X. Li, Decorating Ag/AgCl on UiO-66-NH_2: Synergy between Ag plasmons and heterostructure for the realization of efficient visible light photocatalysis, Chin. J. Catal. 40 (2019) 1187–1197, https://doi.org/10.1016/S1872-2067(19)63377-2.

[59] R.R. Solís, M. Peñas-Garzón, C. Belver, J.J. Rodriguez, J. Bedia, Highly stable UiO-66-NH_2 by the microwave-assisted synthesis for solar photocatalytic water treatment, J. Environ. Chem. Eng. 10 (2022), 107122, https://doi.org/10.1016/J.JECE.2021.107122.

[60] M. Peñas-Garzón, M.J. Sampaio, Y.L. Wang, J. Bedia, J.J. Rodriguez, C. Belver, C. G. Silva, J.L. Faria, Solar photocatalytic degradation of parabens using UiO-66-NH_2, Sep. Purif. Technol. 286 (2022), 120467, https://doi.org/10.1016/J.SEPPUR.2022.120467.

[61] J. Long, S.S. Wang, Z. Ding, S.S. Wang, Y. Zhou, L. Huang, X. Wanga, Amine-functionalized zirconium metal–organic framework as efficient visible-light photocatalyst for aerobic organic transformations, Chem. Commun. 48 (2012) 11656–11658, https://doi.org/10.1039/C2CC34620F.

[62] C. Du, Z. Zhang, G. Yu, H. Wu, H. Chen, L. Zhou, Y. Zhang, Y. Su, S. Tan, L. Yang, J. Song, S. Wang, A review of metal organic framework (MOFs)-based materials for antibiotics removal via adsorption and photocatalysis, Chemosphere 272 (2021), 129501, https://doi.org/10.1016/j.chemosphere.2020.129501.

[63] Y. Pi, X. Li, Q. Xia, J. Wu, Y. Li, J. Xiao, Z. Li, Adsorptive and photocatalytic removal of Persistent Organic Pollutants (POPs) in water by metal-organic frameworks (MOFs), Chem. Eng. J. 337 (2018) 351–371, https://doi.org/10.1016/j.cej.2017.12.092.

[64] H. Diarmand-Khalilabad, A. Habibi-Yangjeh, D. Seifzadeh, S. Asadzadeh-Khaneghah, E. Vesali-Kermani, g-C_3N_4 nanosheets decorated with carbon dots and CdS nanoparticles: Novel nanocomposites with excellent nitrogen photofixation ability under simulated solar irradiation, Ceram. Int. 45 (2019) 2542–2555, https://doi.org/10.1016/J.CERAMINT.2018.10.185.

[65] Y. Wang, W. Wei, M. Li, S. Hu, J. Zhang, R. Feng, In situ construction of Z-scheme g-C_3N_4/$Mg_{1.1}Al_{0.3}Fe_{0.2}O_{1.7}$ nanorod heterostructures with high N_2 photofixation ability under visible light, RSC Adv. 7 (2017) 18099–18107, https://doi.org/10.1039/C7RA00097A.

[66] Y. Zhang, Y. Ma, L. Wang, Q. Sun, F. Zhang, J. Shi, Facile one-step hydrothermal synthesis of noble-metal-free hetero-structural ternary composites and their application in photocatalytic water purification, RSC Adv. 7 (2017) 50701–50712, https://doi.org/10.1039/C7RA10732C.

[67] X. Xin, T. Xu, J. Yin, L. Wang, C. Wang, Management on the location and concentration of Ti^{3+} in anatase TiO_2 for defects-induced visible-light photocatalysis, Appl. Catal. B 176–177 (2015) 354–362, https://doi.org/10.1016/J.APCATB.2015.04.016.

[68] X.D. Du, X.H. Yi, P. Wang, W. Zheng, J. Deng, C.C. Wang, Robust photocatalytic reduction of Cr(VI) on UiO-66-NH_2(Zr/Hf) metal-organic framework membrane under sunlight irradiation, Chem. Eng. J. 356 (2019) 393–399, https://doi.org/10.1016/J.CEJ.2018.09.084.

[69] R. Liu, S. Meng, Y. Ma, L. Niu, S. He, X. Xu, B. Su, D. Lu, Z. Yang, Z. Lei, Atmospherical oxidative coupling of amines by UiO-66-NH_2 photocatalysis under milder reaction conditions, Catal. Commun. 124 (2019) 108–112, https://doi.org/10.1016/J.CATCOM.2019.03.011.

[70] P.M. Wood, The potential diagram for oxygen at pH 7, Biochem. J 253 (1988) 287–289, https://doi.org/10.1042/BJ2530287.

[71] W.H. Koppenol, D.M. Stanbury, P.L. Bounds, Electrode potentials of partially reduced oxygen species, from dioxygen to water, Free Radic. Biol. Med. 49 (2010) 317–322, https://doi.org/10.1016/J.FREERADBIOMED.2010.04.011.

[72] M.S. Alam, B.S.M. Rao, E. Janata, ·OH reactions with aliphatic alcohols: Evaluation of kinetics by direct optical absorption measurement. A pulse radiolysis study, Rad. Phys. Chem. 67 (2003) 723–728, https://doi.org/10.1016/S0969-806X(03)00310-4.

[73] E.M. Rodríguez, G. Márquez, M. Tena, P.M. Álvarez, F.J. Beltrán, Determination of main species involved in the first steps of TiO_2 photocatalytic degradation of organics with the use of scavengers: The case of ofloxacin, Appl. Catal. B 178 (2015) 44–53, https://doi.org/10.1016/j.apcatb.2014.11.002.

[74] P.S. Rao, E. Hayon, Redox potentials of free radicals. IV. Superoxide and hydroperoxy radicals $\cdot O_2^-$ and $\cdot HO_2$, J. Phys. Chem. 79 (2002) 397–402, https://doi.org/10.1021/J100571A021.

[75] B.H.J. Bielski, D.E. Cabelli, R.L. Arudi, A.B. Ross, Reactivity of HO_2/O_2^- radicals in aqueous solution, J. Phys. Chem. Ref. Data 14 (1985) 1041–1100, https://doi.org/10.1063/1.555739.

[76] C.L. Greenstock, R.W. Miller, The oxidation of tiron by superoxide anion. Kinetics of the reaction in aqueous solution and in chloroplasts, Biochim. Biophys. Acta 396 (1975) 11–16, https://doi.org/10.1016/0005-2728(75)90184-X.

[77] C.K. Huang, T. Wu, C.W. Huang, C.Y. Lai, M.Y. Wu, Y.W. Lin, Enhanced photocatalytic performance of $BiVO_4$ in aqueous $AgNO_3$ solution under visible light irradiation, Appl. Surf. Sci. 399 (2017) 10–19, https://doi.org/10.1016/j.apsusc.2016.12.038.

[78] A.M. Chávez, A. Rey, J. López, P.M. Álvarez, F.J. Beltrán, Critical aspects of the stability and catalytic activity of MIL-100(Fe) in different advanced oxidation

processes, Sep. Purif. Technol. 255 (2021), 117660, https://doi.org/10.1016/j.seppur.2020.117660.
[79] D. Zou, D. Liu, Understanding the modifications and applications of highly stable porous frameworks via UiO-66, Mater. Today Chem. 12 (2019) 139–165, https://doi.org/10.1016/J.MTCHEM.2018.12.004.
[80] D. Bůžek, S. Adamec, K. Lang, J. Demel, Metal-organic frameworks vs. buffers: Case study of UiO-66 stability, Inorg. Chem. Front. 8 (2021) 720–734, https://doi.org/10.1039/d0qi00973c.
[81] Y. Chen, X. Zhang, L. Mao, Z. Yang, Dependence of kinetics and pathway of acetaminophen photocatalytic degradation on irradiation photon energy and TiO_2 crystalline, Chem. Eng. J. 330 (2017) 1091–1099, https://doi.org/10.1016/J.CEJ.2017.07.148.
[82] M. Peñas-Garzón, A. Gómez-Avilés, C. Belver, J.J. Rodriguez, J. Bedia, Degradation pathways of emerging contaminants using TiO_2-activated carbon heterostructures in aqueous solution under simulated solar light, Chem. Eng. J. 392 (2020), 124867, https://doi.org/10.1016/J.CEJ.2020.124867.